Laboratoire de Physique III

Creating tutorials to make beautiful Astronomical images with TELESTO

Student: Camille De Decker

Supervisors: Prof. Francesco Pepe
Maddalena Bugatti

UNIVERSITÉ DE GENÈVE

FACULTÉ DES SCIENCES
Département d'astronomie

Academic years : 2024 - 2025

Table of Contents

1 Introduction

1.1 Historical context of astronomical imaging

The observation of celestial objects has always been at the heart of astronomy, acting as a gateway to understanding our universe. This practice dates back to prehistoric times, when early humans were already recording lunar cycles through carvings, as highlighted by American archaeologist Alexander Marshack (Hayden et al. (2011), Marshack (1964)). While these early observations were rudimentary, the evolution of astronomical practices significantly accelerated over the centuries, particularly from Antiquity onwards, when Greek astronomers such as Euclid and Ptolemy laid the foundations of instrumental astronomy with their work on optical properties (Eecke et al. (1938), Ptolemy et al. (1996)).

Progress in sky observation took a major step forward with the invention of the astronomical telescope, the first demonstration of which was made in 1608 by the Dutch scientist Hans Lippershey. However, it was Galileo who, in 1610, with his improved telescope, revolutionized astronomy by publishing Sidereus Nuncius (Galilei (2016)), a work in which he first described the moons of Jupiter and mapped constellations such as Orion and the Pleiades. A year later, Kepler would improve upon this model, constructing the astronomical telescope as we know it today. It was this model that allowed astronomy to evolve, enabling the observation of celestial objects with greater precision.

The improvement of observation instruments continued with the invention of the reflecting telescope, proposed by James Gregory in 1663, which replaced lenses with concave mirrors, overcoming the limitations of astronomical telescopes by reducing chromatic aberrations. Today, however, it is Newton's telescope that is the most well-known, built in 1668, just before Gregory's. This telescope enabled the transition from observing the solar system and very bright stars to more detailed observation of deep space: nebulae, galaxies, star clusters.

Over the years, increasingly powerful telescopes were built, such as Herschel's in 1789, followed by Rosse's in 1845, and then ever larger instruments such as the Hale telescope (1.5 meters) at Mount Wilson Observatory in 1908, and the Hooker telescope in 1917 (2.5 meters). Today, the Gran Telescopio Canarias (GTC) located on the island of La Palma, with its 10.4-meter mirror, is the largest operational telescope, while awaiting the ELT (Extremely Large Telescope) with its future 39-meter mirror.

Alongside this instrumental evolution, a desire to preserve celestial images emerged, leading to major innovations. The invention of the daguerreotype in 1839 by Louis Daguerre made it possible to capture images of celestial objects, starting with the photograph of the Moon taken by John William Draper in 1840 (Gillespie (2012)). This process, based on a copper plate sensitized with iodine vapors and developed by mercury vapor fixation, allowed photography to extend to more distant objects, such as the star Vega in 1850 and nebulae starting in the 1880s. However, the complexity of this technique gave way to simpler and more reproducible methods, such as the photographic plates developed by George Eastman (founder of Kodak), which were used and modernized until the 1980s in observatories. It was the invention of the CCD sensor in 1969 by AT&T Laboratories and Bell Telephone (which earned W.S. Boyle and G.E. Smith the Nobel Prize in 2009) that marked the end of the use of photographic plates and opened a new era in the capture of astronomical images.

1.2 Astronomical imaging sensors: CMOS and CCD

The CCD (Charge-Coupled Device) sensor and the CMOS (Complementary Metal-Oxide Semiconductor) sensor, invented by Eric Fossum in 1993, have revolutionized astrophotography. Although they share a common goal, their operation differs significantly (Magnan (2003)).

One can imagine the CCD sensor as a matrix composed of many elements, each consisting of a MOS (Metal-Oxide-Semiconductor) capacitor, which includes a photosensitive area, semiconductor elements, and an insulator. Each pixel (element of the grid) is thus capable of detecting photons. When a photon, whose energy is greater than the band gap of the semiconductor, strikes the element, it generates an electric charge. This charge, proportional to the received light intensity, is then transferred from one pixel to another within the matrix, following a given direction, until it reaches a central capacitor. This capacitor converts the accumulated charge into a voltage. After amplification, this voltage is then converted into a digital signal outside the CCD matrix.

In contrast, the CMOS sensor operates differently. When a photon interacts with a semiconductor element in a CMOS pixel, the resulting charge is directly converted into voltage at the same pixel, thanks to an amplifier integrated into each pixel. This conversion allows for rapid and independent reading for each pixel. The sum of all the individual pixel voltages then generates a global voltage, which, as with the CCD, can be converted into a digital signal by an analog-to-digital converter located outside the sensor matrix.

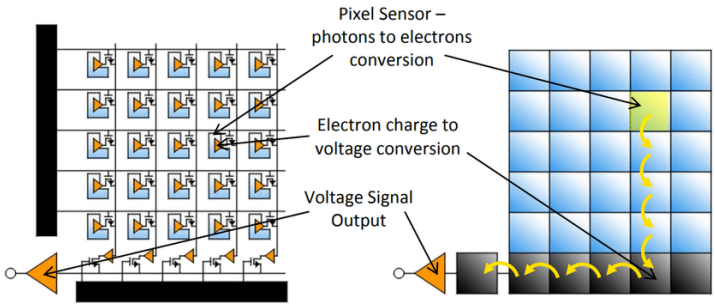

Figure 1: Comparison of CMOS (left) and CCD (right) Sensor Operation (Topac (2018)).

Thus, each technique has its advantages and disadvantages. The CCD tends to be more power-hungry but allows for higher-quality images, while the CMOS is more energy-efficient and faster in image processing, but the presence of an amplifier at each pixel reduces spatial resolution.

1.3 Systematic artifacts in image acquisition

In astrophotography, the quality of images depends on several factors, such as environmental conditions, the optics used, and the acquisition system. While the first are beyond our control, the optics and the acquisition system can introduce distortions and artifacts that can be corrected through appropriate image processing. The following sections detail these anomalies (Howell (2000)).

1.3.1 Electronic noise

The first type of anomaly generated by the acquisition system is electronic noise. This noise is always present and primarily arises from the conversion and amplification of electronic charges into voltage. For the CCD sensor, this conversion is carried out centrally, whereas for the CMOS, each pixel performs this conversion independently. Another noise factor is what is called the "positive offset." Indeed, the ADC (Analog-to-Digital Converter), which converts the charges into a digital signal, generates values that are always positive. This systematic voltage offset is applied to ensure that pixel values are always positive, despite fluctuations due to noise that could theoretically be negative. This set of phenomena is commonly referred to as "Read-out noise" and manifests as an erratic distribution of pixels that have no relation to the observed celestial object. It is worth noting that this electronic noise is also amplified by interference from surrounding electronic components, which generate additional disturbances that directly affect the sensor.

1.3.2 Thermal noise

In addition to electronic noise, there is also thermal noise, which is directly related to the sensor's temperature. When the sensor is located in an environment with a temperature above absolute zero, the electrons in the semiconductor materials gain kinetic energy due to thermal agitation. This energy allows some electrons to overcome the semiconductor gap and reach the conduction band, thus generating a signal similar to that of photons. This phenomenon, known as "dark current", depends exponentially on temperature and increases with exposure time.

1.3.3 Optical noise

Finally, another systematic anomaly is related to the optical aberrations of the system. Lenses or other optical elements may have imperfections, such as spots, dust, or scratches, which affect the quality of the image. Additionally, there may be a phenomenon known as "vignetting," which refers to a reduction in brightness at the edges of the image. This phenomenon is caused by the variation in light intensity based on the viewing angle, often due to the design of the optics or obstacles that alter the peripheral light flow.

The objective of this laboratory is therefore to develop a Python code (in a Jupyter notebook) capable of processing astronomical images to correct these various anomalies.

2 Method

2.1 Materials

We will be working with images acquired using the Telesto telescope (TELescope for Science, Teaching, and Outreach), which is the telescope at the Geneva Observatory. It is a reflecting telescope (Figure 2) with a 60 cm diameter mirror, equipped with a CMOS sensor (16 bits) and a focal ratio of 3.8, making it particularly suitable for deep sky observation and wide-field astronomy. Telesto is mounted on an equatorial mount, and its movement is computer-controlled.

Figure 2: Photo of the Telesto Telescope Model.

Its configuration is that of a slightly modified Cassegrain-type telescope (Figure 3): the incoming light strikes a concave parabolic primary mirror, which focuses and directs the rays toward a secondary mirror (non-parabolic in this modified Cassegrain configuration), which in turn reflects the rays toward a set of corrective lenses through a central hole drilled in the primary mirror, and the image forms in the focal plane where, in our case, the CMOS sensor is placed.

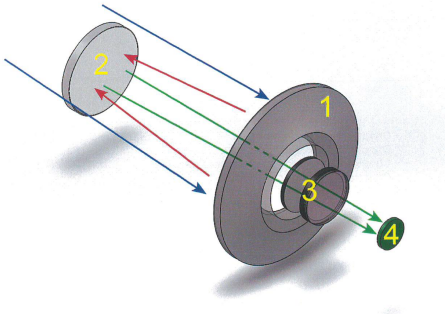

Figure 3: Diagram of the optical path taken by the light: in 1 we find the concave mirror, in 2 the secondary mirror, in 3 the group of corrective lenses and in 4 the focal plane.

The body of the telescope is surrounded by a black cloth to limit interactions with the surrounding light, and a cover can be added to isolate it from the incident light.

In our setup, a filter wheel is placed just before the CMOS sensor. This wheel includes nine filters (Figure 4): some filters from the Johnson-Kron-Cousin system: red (R), blue (B), visual (V), and infrared (I); related filters with narrower and more intense transmission spectra: g', r', and i'; an L filter (which cuts IR and UV signals), and finally an H-alpha filter.

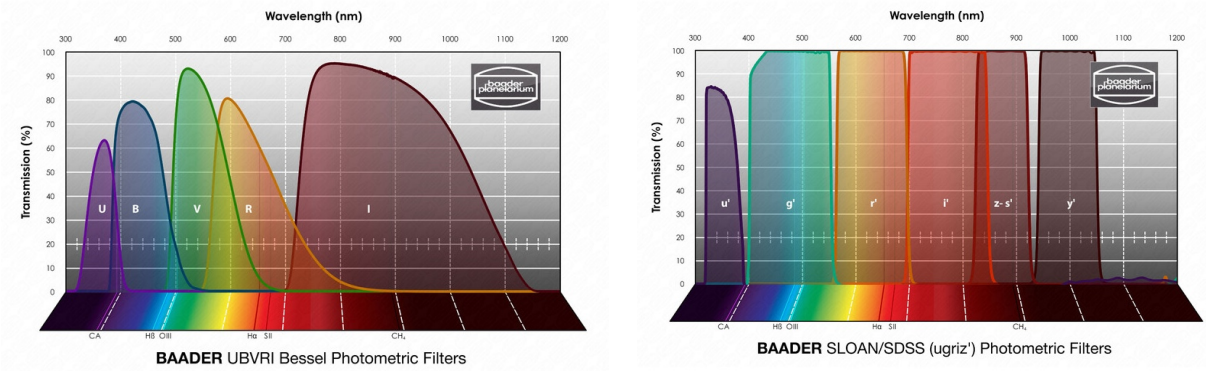

Figure 4: Examples of Filter Transmissions Obtained with the Filter Wheel.

During our solar observations, a solar filter is placed on a peripheral opening of the cover. This filter allows only 1/10,000 (measured on an optical bench) of the incident radiation to pass through.

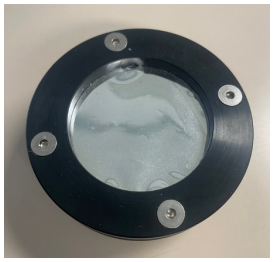

Figure 5: Photo of the Solar filter.

An important computer interface is required to control Telesto. Indeed, it is necessary to control the movement of its mount and dome when aiming at a celestial object (and thus locating it in space) and its focus. These settings are managed through various systems: the OSBus controller, which allows for focusing, the MAESTRO software, which controls the Astrometric Telescope Control System (ATCS) – the system that enables the mount to locate and move based on the objects pointed to in the celestial sphere. Finally, the SkyX user interface allows control of image acquisition, filter selection, automatic movement of the focus, dome, and, of course, the telescope based on the targeted objects.

2.2 Observed objects

In order to build and test the code, observations of the Sun, Andromeda, and Saturn were carried out. Statistical analyses were performed on the Sun data.

2.3 Code development workflow

Before starting, it was essential to define the objectives of the code: to enable Telesto users to easily process their science frames to obtain images with minimal artifacts, suitable for analysis. The code must be user-friendly, efficient enough to process several dozen images, and ensure reproducible results.

2.3.1 Data preparation

The first step of the code is to import the necessary libraries, as well as the shortcuts used throughout the processing (see the appendixes). Next, a cell allows the user to specify the paths to the different folders containing the data. Finally, two cells are included to visualize the files in these folders and count them, thus making it easier for the user to locate them.

2.3.2 Bias frame correction

The first correction to be made concerns the electronic noise, which can be corrected by creating "Bias Frames". The idea is to capture an image representing the characteristic electronic noise of the system, so it can later be subtracted from the other frames. To do this, several exposures are taken (at least ten (Howell (2000))), with an exposure time of zero seconds. This precaution is essential to avoid introducing artifacts related to other phenomena, such as dark current (*cf.* section 2.2.3). Additionally, the cover is kept in place to ensure that the charges accumulated in the photosensitive elements reflect only the electronic noise. The images obtained are then combined into a "Master Bias Frame" (MBF).

Bias Frames can be analyzed statistically. Since the electronic noise is due to random variations, it generally follows a Gaussian distribution (though not always (Merline et al. (1995))), although

it is not centered at zero due to the systematic positive offset. The standard deviation of this distribution allows for an assessment of the noise level.

In our case, ten Bias Frames were captured, and the statistical data was verified (example for one Bias Frame shown in Figure 6).

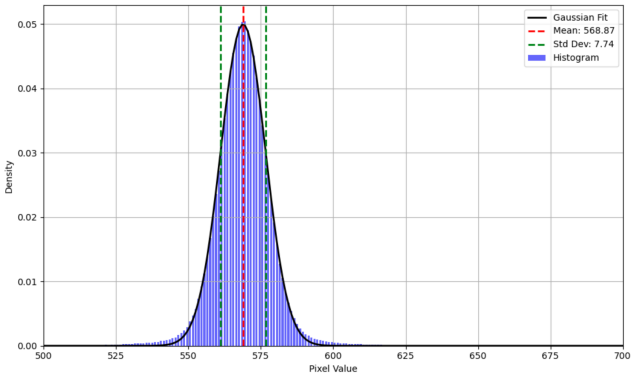

Figure 6: Gaussian fit of raw bias frame data.

For the bias frames, as well as for all the combinations of frames we will discuss later, three main combinatory methods are commonly used: the mean, the median, and a hybrid method combining one of these with "clipping" (which involves limiting the impact of extreme values by excluding them or replacing them with values near the specified bounds). The median, with or without clipping, is often preferred over the mean because it is less sensitive to extreme values and effectively eliminates transient artifacts. However, the median is not without its drawbacks: for a large number of images without outliers, it is less effective than the mean at reducing random noise. Additionally, if the point spread function (PSF) varies from one image to another, combining using the median method can worsen this distortion by producing an incoherent PSF, limiting its usefulness in certain sensitive analyses (Gruen et al. (2014)).

In our case, where the Bias Frames almost perfectly follow Gaussian distributions and therefore exhibit few extreme values, the two methods (as shown in Figure 7) yield statistically similar results (though it can be noticed, in the graph of the combinatory method using the mean, that the Gaussian is less symmetric compared to that of the median).

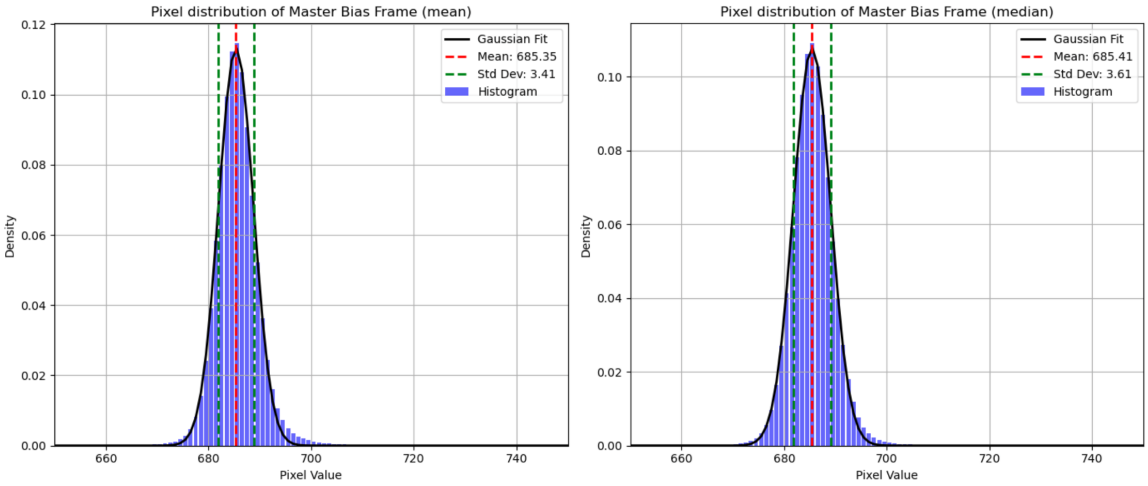

Figure 7: Comparison of Mean and Median Methods for Combining Bias Frames.

In terms of execution time, the mean method is significantly faster (1.78 s vs. 19.64 s), which leads us to choose this method. We also opted for a manually defined mean function rather than using `np.mean` to further optimize execution time (1.78 s vs. 11.81 s). The Figure 8 presents the obtained MBF.

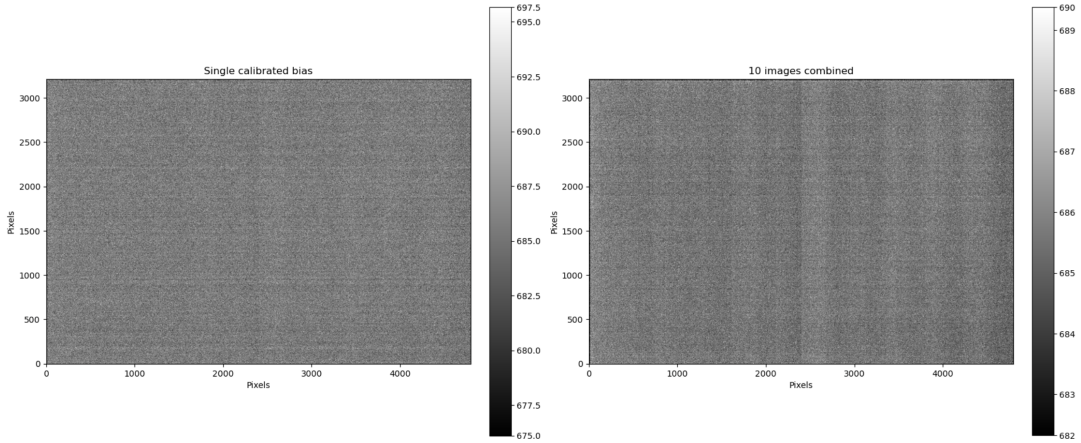

Figure 8: Comparison Between Raw and Combined Bias Frame Images.

2.3.3 Dark frame correction

To correct for thermal noise, it is recommended to take images (the recommended number varies according to publications, but it is generally accepted that around twenty images constitutes a minimum (Ashley (2015))) with the cover in place and an exposure time identical to that of the future light frames. These images, called "Dark Frames," reflect the thermal noise that will affect the light frames. It should be noted that these dark frames also contain the electronic noise from the bias frames discussed in section 2.3.2, as electronic noise is always present when taking images, regardless of their nature. Before combining the dark frames to create a "Master Dark Frame" (MDF), it is therefore recommended to subtract the MBF.

Theoretically, it would be possible not to subtract the MBF from the dark frames, thus obtaining a "cumulative" MDF (MDFc) that would directly include the contribution of the bias frames. However, this approach is not advised because it would prevent the subtraction of the "positive offset" from the light frames when using the MDFc. Additionally, it is common for the light frames to have a different exposure time than the dark frames. In such cases, the dark frames need to be adjusted to match the exposure time of the light frames. Using an MDFc would also require adjusting the exposure time of the bias frame, which is undesirable because the bias frame should be taken with an exposure time as close as possible to zero seconds. Therefore, this method is less flexible in case of future modifications.

To study the impact of the most common filters on the combination of dark frames, thirty dark frames were taken (ten for each filter: B, V, and R). The combination was performed using the mean method on all thirty dark frames together, then separately for each filter. This approach allowed comparing the statistical data for each case:

	Image Name	Median	Mean	S.D.
0	Master Dark Frame B	9.0	12.701889	235.824028
1	Master Dark Frame R	5.5	8.822799	233.512682
2	Master Dark Frame V	3.0	6.757747	234.671831
3	Master Dark Frame (median)	5.5	9.017603	234.456375

Figure 9: Statistical Analysis of Different MDF Combinations as a Function of Filter.

The disparity observed in the means and medians of the dark frames for the different filters is surprising. Theoretically, these frames should only reflect uniform electronic noise, as no photons should reach the sensor. This anomaly suggests the possibility that stray light may have excited the CMOS sensor through the different filters.

Based on this hypothesis, we can analyze the sensor's response depending on the filters used. First, it is well-established that the CMOS sensor does not exhibit linear quantum efficiency (Alarcon et al. (2023)). It is notably more sensitive to photons with wavelengths between 420 and 540 nm, peaking at 500 nm (i.e., in the blue-green range). Additionally, transmissions vary across filters: the V filter has an average transmission of 64% with a quantum efficiency of 78%, the B filter has an average transmission of 56% with a quantum efficiency of 80%, and the R filter has an average transmission of 54% with a quantum efficiency of 60% (*Baader UBVRI Filter – Transmission* - (2024)). Therefore, we would expect the mean and median pixel values for the MDF with the V filter to be higher than those for the B filter (with transmission around 50% versus 45%), and these in turn higher than those for the R filter. However, this is not the case here, with the V filter showing the lowest mean and median of the set. One could hypothesize the presence of dust on the V filter or inconsistencies in the transmission of the mirrors for these wavelengths.

To evaluate the impact of different combinatory methods for the dark frames, a statistical analysis (Figures 10 and 11) was performed.

	Dark Frame Type	Mean	Median	S.D.	Min	Max
0	Mean	9.710530	6.224561	223.678624	-91.630702	61506.974283
1	Median	9.017603	5.500000	234.456375	-91.500000	64864.000000
2	Clipping	9.017119	5.500000	234.436989	-91.500000	64864.000000

Figure 10: Statistical Analysis of Different MDF Combinations.

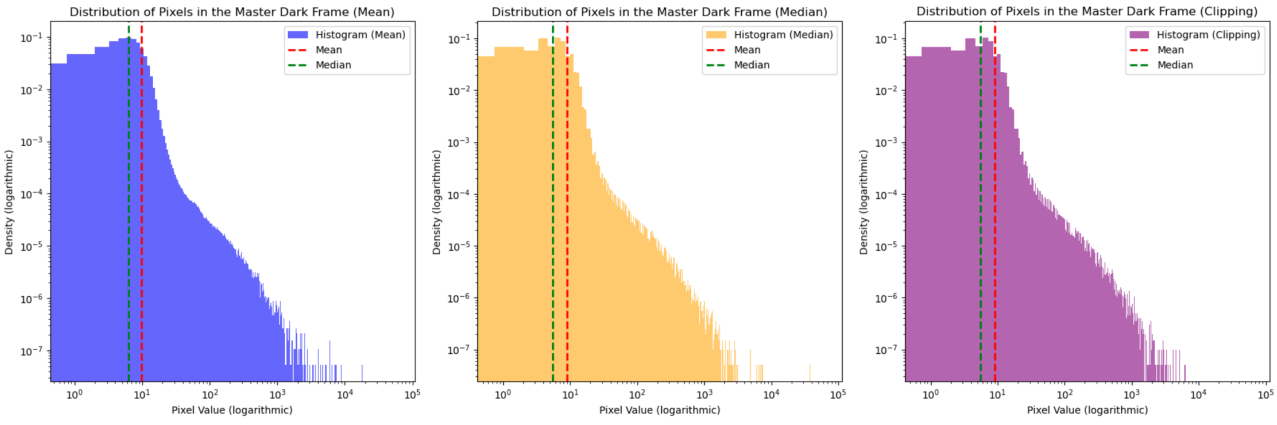

Figure 11: Comparison of Different MDF Combinations.

The results show little variability between the methods but significant differences in execution times: 84 s (mean), 164 s (median), and 625 s (sigma-clipping). The manual implementation of the code to average the dark frames showed an even shorter execution time, making this method the preferred choice. The Figure 12 shows the resulting MDF.

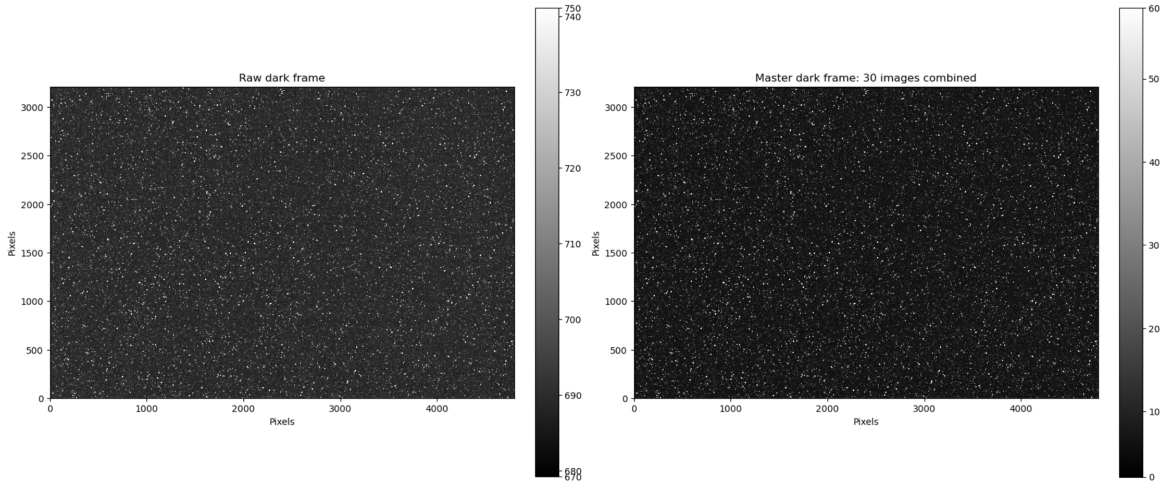

Figure 12: Comparison Between Raw and Combined Dark Frame Images.

2.3.4 Flat frame correction

Finally, the "optical" defects are corrected using "Flat Frames." To obtain these images, at least five photographs of the sky must be taken (Howell (2000)) at a time when the brightness is considered uniform (for example, at dawn or dusk), with an exposure time sufficient to sensitize each pixel without saturating them: it is commonly accepted that the exposure should be about 2/3 of the sensor's dynamic range (around 40,000 counts for the full 16-bit scale). Since flat frames are affected by electronic and thermal noise, it is crucial to subtract the MBF and MDF from them. The MDF should also be calibrated to match the same exposure time as the flat frames before their subtraction. Once this processing is done, the flat frames need to be normalized before combining them to create the Master Flat Frame (MFF). Normalization is important because the sensor may have a non-uniform response across its surface, leading to global variations in brightness between the flat frames. This step ensures that each flat frame contributes equally to the creation of the MFF and helps avoid artifacts in the combination that might affect the correction of optical aberrations.

Since the light frames may be taken with different filters, and optical aberrations depend on the optical path, it is important to create a distinct MFF for each filter.

An analysis of the different techniques for combining flat frames was also performed:

	Flat Frame Type	Mean	Median	S.D.	Min	Max
0	Mean	0.621890	0.628498	0.056640	-0.333381	0.786055
1	Median	0.585911	0.592050	0.053457	-0.580606	0.805075
2	Clipping	0.621759	0.628365	0.056606	-0.160377	0.805075

Figure 13: Statistical Analysis of Different MFF Combinations.

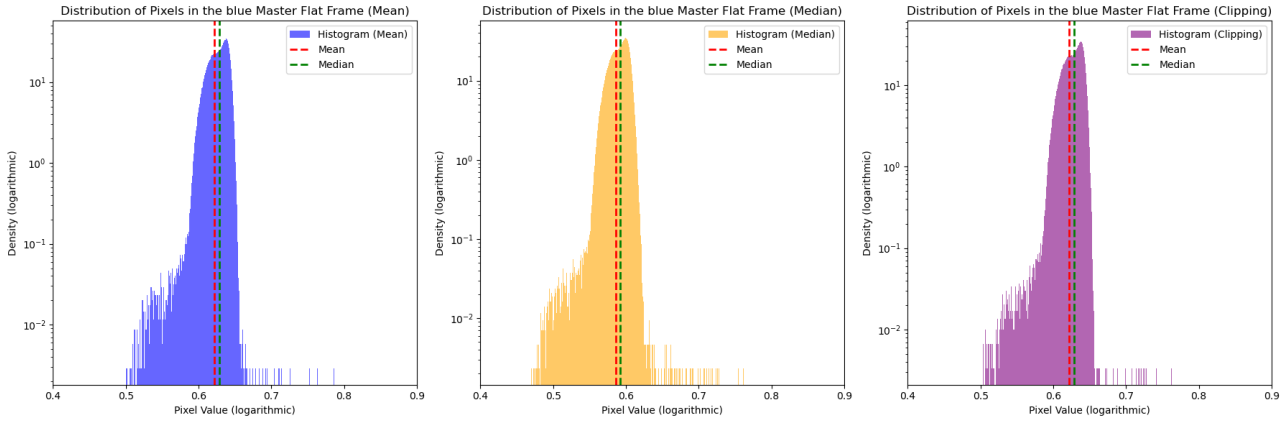

Figure 14: Comparison of Different MFF Combinations.

It can be observed (Figure 13) that the standard deviation is lower in the case of the median, although this difference is modest. As in the other cases, the combination method was chosen based on the best trade-off between quality and execution time. Thus, the averaging method, which executes in 59 s (compared to 120 s or even 25 minutes for other methods), was selected. An example of the MFF is presented in Figure 15 (V filter).

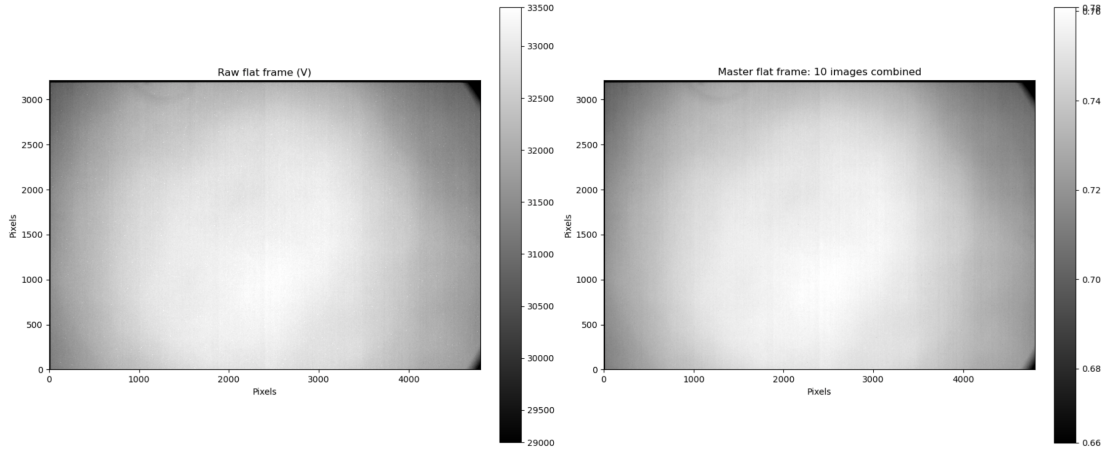

Figure 15: Comparison Between Raw and Combined Flat Frame Images.

2.3.5 Final calibration and combination

The final step of this image pre-processing involves combining the light frames after their correction using the various calibration frames: subtraction of the MBF, the MDF (adjusted to the exposure time of the light frame), and division by the MFF corresponding to the filter used (Figure 16).

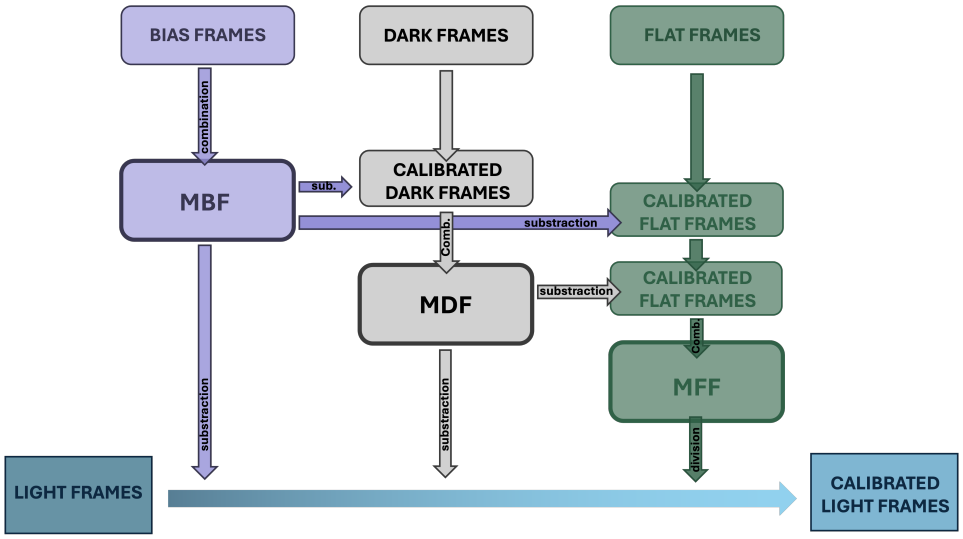

Figure 16: Calibration process for light frames.

However, this step presents a technical challenge: the presence of zero-valued pixels in the MFF. Without adjustment, these pixels would lead to divisions by zero, generating NaN values (i.e., undefined values), making the images difficult to process. To prevent these anomalies, the zero-valued pixels were replaced with a very small value (10^{-6}). However, this correction introduced a new problem: division by such a small value caused pixels to exceed the physical limits of the sensor's brightness. Additionally, the subtraction of the various bias frames also resulted in pixels with negative values, which are physically meaningless. To correct these anomalies, a function was integrated into the code that replaces these problematic pixels with the average value of the eight surrounding pixels.

Once the light frames were calibrated, the combination of images became a key step in improving the overall signal. Two combinatory methods were tested: one using the median and one using the mean. The initial median-based method, although effective and fast (55 s for the mean versus 60 s for the median), did not take object tracking into account. While this flaw has little impact for images of the Sun, observed over a short period of time, it becomes noticeable for objects like Andromeda, where the movement of the celestial sphere causes a perceptible blur in the central image of Figure 17 (exacerbated by poor focus). This issue is improved by using a tracking-based method, where the brightest object in the image is followed (right image of Figure 17).

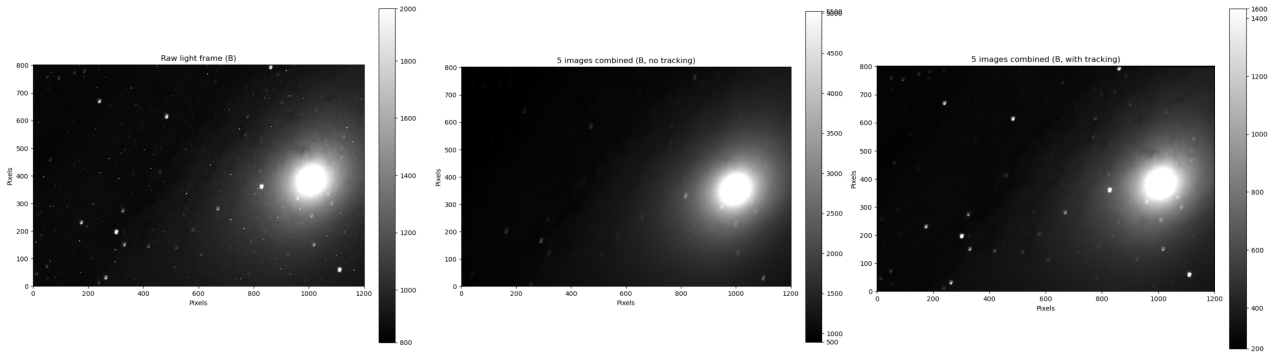

Figure 17: Raw Image Comparison with Median and Tracking-Combined Light Frames.

The median was ultimately chosen for the final combination, as it effectively removes outliers without a significant increase in execution time (196 s versus 204 s for the mean).

	Light Frame (B) Type	Mean	Median	S.D.	Min	Max
0	Tracking (Mean)	8979.348801	4380.838771	6947.315545	17.276594	58363.104460
1	Tracking (Median)	8978.469323	4380.036010	6946.966859	505.737614	22479.751108

Figure 18: Statistical Analysis of Different Combinations of Light Frames.

The statistical analysis (Figures 18 and 19) confirms this effectiveness. As shown in Figure 19 (right), the most extreme pixel values were ignored, revealing two distinct regions: the first, up to about 8000 counts, corresponds to the background, and the second is attributed to the observed object. An example of the resulting image is presented in Figure 20. This image shows little significant improvement, an aspect that will be discussed in more detail in section 3.0.1.

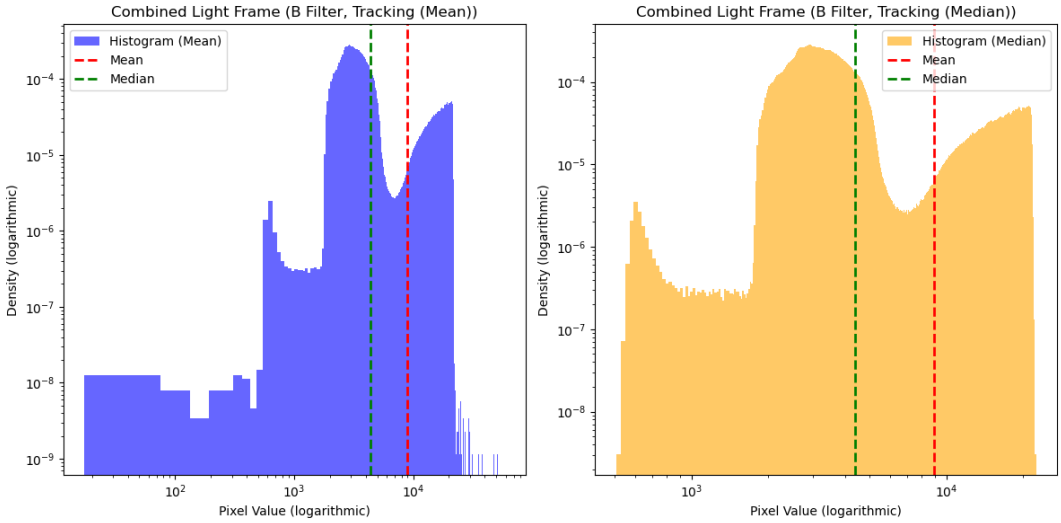

Figure 19: Comparison of Different Combinations of Light Frames.

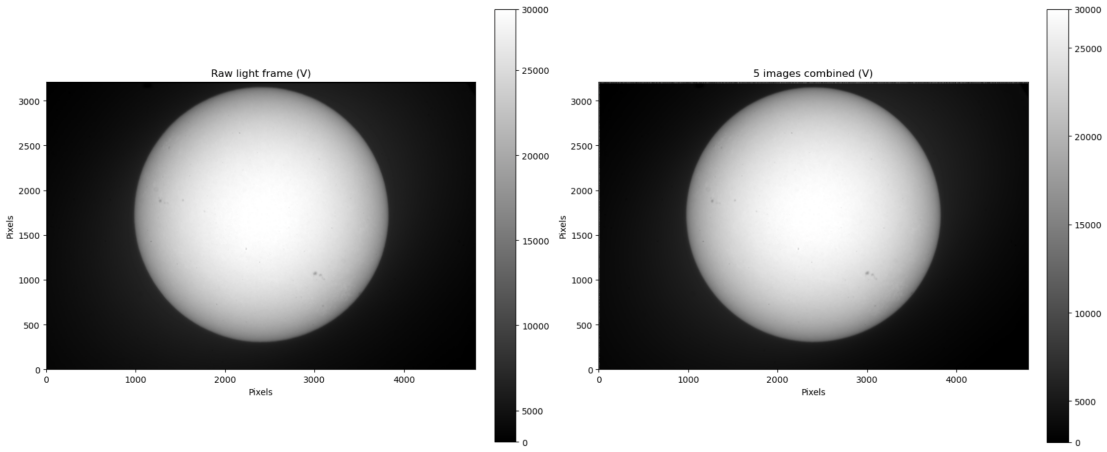

Figure 20: Comparison Between Raw and Combined Light Frame Images.

2.3.6 Image visualization

A final section was added to the code to allow the user to visualize, color, and save their images. If combined light frames for the R, V, and B filters are available, it is also possible to generate an RGB (Red-Green-Blue) image. This process includes a function for overlaying the images based on the center of the object of interest. Without this adjustment, the edges of the object show a shift between the colored filters, as shown in Figure 21.

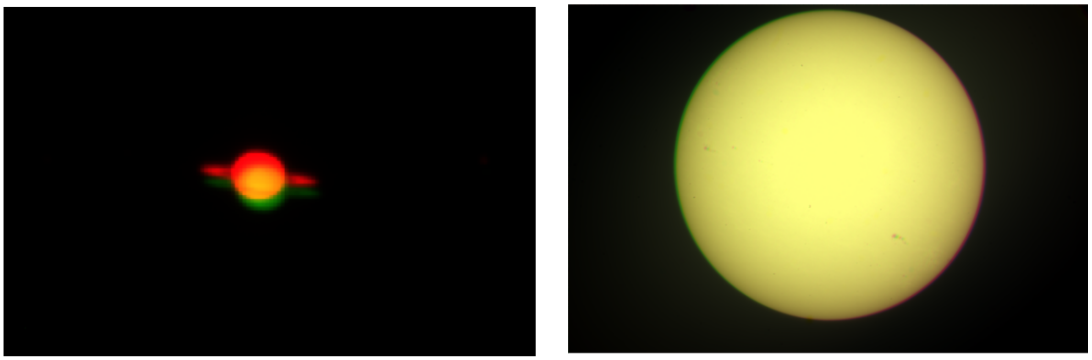

Figure 21: RGB Composite of Saturn and the Sun without Tracking.

3 Results and discussion

After processing the images, here are a few examples obtained:

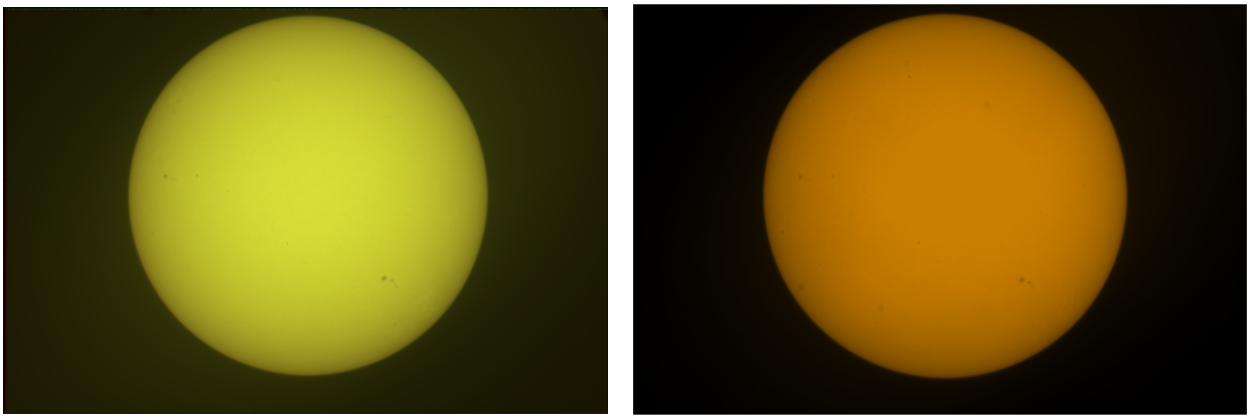

Figure 22: RGB Composite (left) and H-alpha Filtered Image (right) of the Sun.

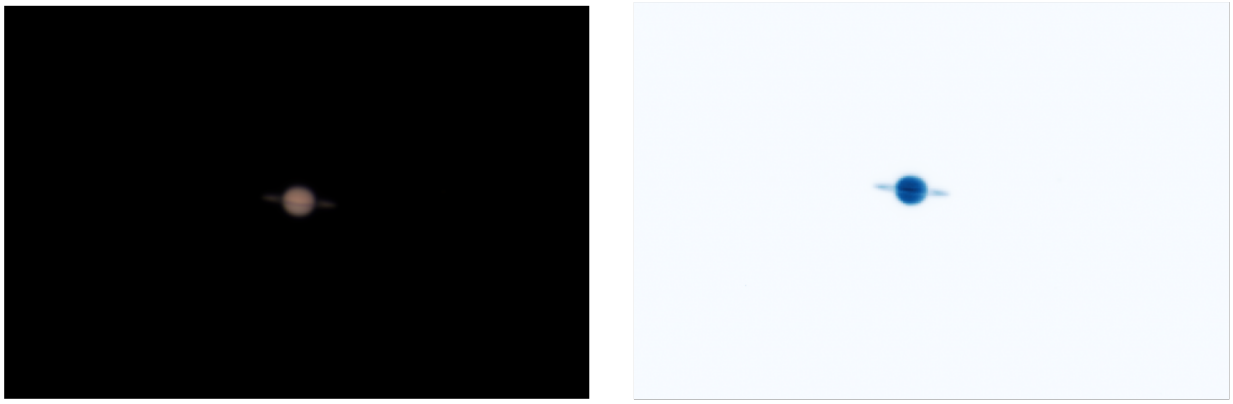

Figure 23: RGB Composite (left) and Blue Filtered Image (right) of Saturn.

Thanks to these images, we can determine the real diameter of the celestial object in question, here using Saturn as an example. The difficulty lies in obtaining the diameter of the planet on the image. The simplest technique is direct measurement of this diameter: about 30 pixels. This result, combined with the scale of our telescope's plate (0.34 arcsec for a 1x1 binning: we used a 2x2 binning here), allows us to calculate:

$$D_{saturne} = D_{T-S} \cdot \tan(\theta) \approx D_{T-S} \cdot \theta = 1.224 \cdot 10^9 \cdot \frac{0.34 \cdot 2}{206265} \cdot 30 \approx 121056 \pm 26988 \; km \quad (1)$$

With the uncertainty calculated as follows:

$$\delta D_{\text{Saturne}} = \sqrt{\left(\frac{\partial D_{\text{Saturne}}}{\partial D_p}\delta D_p\right)^2 + \left(\frac{\partial D_{\text{Saturne}}}{\partial p}\delta p\right)^2 + \left(\frac{\partial D_{\text{Saturne}}}{\partial D_{\text{T-S}}}\delta D_{\text{T-S}}\right)^2} \quad (2)$$

Thus,

$$\epsilon_{D_{saturne}} = \frac{|(116464) - (121056)|}{116464} \cdot 100 \approx 4\% \quad (3)$$

Our uncertainty thus intercepts the real value, and the precision seems acceptable.

We could also consider a 2D Gaussian fitting to obtain the standard deviation values in the x and y directions. Thus, the diameter in pixels can be found:

$$D_p = \frac{2\sqrt{2\ln 2}\cdot\sigma_x + 2\sqrt{2\ln 2}\cdot\sigma_y}{2} = \frac{2.3548\cdot 9.00 + 2.3548\cdot 7.36}{2} = 19.25 \pm 0.01\ pixels \quad (4)$$

From which:

$$D_{saturne} \approx 1.224\cdot 10^9 \cdot \frac{0.34\cdot 2}{206265}\cdot 19.25 \approx 77718 \pm 37\ km \quad (5)$$

With the uncertainty calculated as follows:

$$\delta D = \sqrt{\left(\frac{\partial D}{\partial \sigma_x}\delta\sigma_x\right)^2 + \left(\frac{\partial D}{\partial \sigma_y}\delta\sigma_y\right)^2} \quad (6)$$

Thus,

$$\epsilon_{D_{saturne}} = \frac{|(116464) - (77178)|}{116464}\cdot 100 \approx 33\% \quad (7)$$

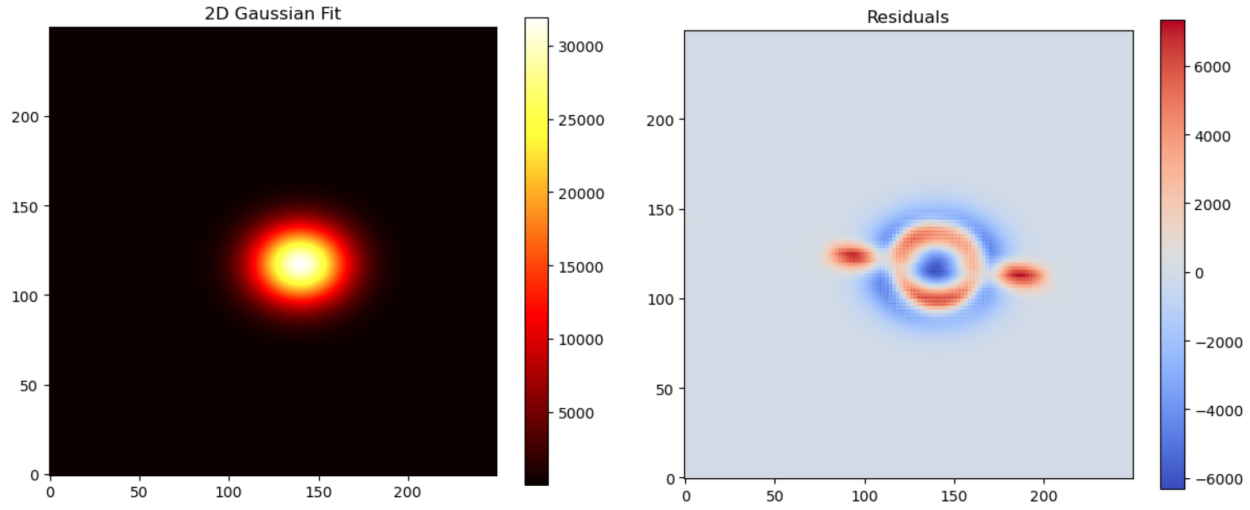

Figure 24: Statistical Analysis of Saturn's Image Data After Gaussian Fitting.

Given these results and Figure 24, we can observe that the Gaussian model, although widely used, does not perfectly capture the shape of Saturn. The planet has a spherical shape that could be better described by a different function, and fine details, such as the edges of the rings, are not represented by a simple Gaussian. Moreover, the inherent blur in the image further complicates the fitting. This leads to an imprecision in the delineation of the object, which partly explains the difficulty in fitting its contour.

Finally, it is possible to use a method that detects the edges of the object using the Canny algorithm (Figure 25), and then fits a circle around the largest contour. With this method, we obtain $D_p = 27.87 \pm 1.62\ pixels$
Hence:

$$D_{saturne} \approx 1.224 \cdot 10^9 \cdot \frac{0.34 \cdot 2}{206265} \cdot 27.87 \approx 112461 \pm 6537\ km \quad (8)$$

Thus,

$$\epsilon_{D_{saturne}} = \frac{|(116464) - (112461)|}{116464} \cdot 100 \approx 3\% \quad (9)$$

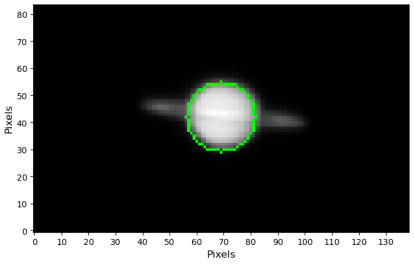

Figure 25: Saturn's Image with Canny Edge Detection.

This method is therefore the most efficient and scientifically accurate among all the methods evaluated.

3.0.1 Challenges in image acquisition: impact of environmental and technical factors

Before discussing the quality of the created notebook, it is essential to examine the quality of the raw images obtained, as they directly influence the effectiveness of the applied processing steps. In general, the autumn season made observations more challenging, mainly due to frequent and significant cloud cover. This limited the simultaneous capture of calibration images (bias, dark, and flat frames) and light frames, affecting the overall consistency of the processing performed.

Certain errors during image capture also had a significant impact on the final results. For example, the movement of the solar filter between the capture of the flat frames and the light frames of the Sun generated noticeable optical aberrations in the final images (Figure 20). Similarly, due to time constraints, the flat frames for the H Alpha filter were taken with insufficient exposure time, leading to pixel values lower than one-third of the sensor's dynamic range. This error made optical correction less effective for these images. Moreover, inadequate focusing for the Andromeda images, combined with unfavorable observation conditions (cloud presence), rendered these images practically unusable for testing the code (Figure 17).

Technical issues also complicated acquisitions. At the end of October, malfunctions of the optical fibers of the Telesto telescope extended the observation sessions. Additionally, it is likely that some dark frames were contaminated by stray light (Figure 9). Indeed, the telescope body is covered with a black cloth that is not entirely opaque, and it was easy to observe that light leaked through the junction between the wall and the dome structure when it was closed, potentially reaching the camera sensor.

3.0.2 Evaluation of image processing strategies

The processing of raw images was carried out by seeking a balance between the statistical quality of the data and the execution time of the code. For the calibration steps (bias, dark, and flat frames), the combinatorial method using the average was favored over the median. This approach allowed for similar results in terms of corrected pixel statistics while significantly reducing processing times. However, it is important to note that this decision was made based on a limited set of images. In the case of an acquisition with a larger number of images

containing aberrations, the use of the median would provide a notable advantage, especially in eliminating extreme values.

For the combination of light frames, a different method was adopted: the images were aligned using automatic tracking of the brightest object in each frame, then combined using the median. This approach yielded satisfactory results for isolated and bright objects, such as the Sun, Saturn, and Andromeda. However, this method has several potential limitations. First, its effectiveness was not tested on less luminous or less distinct targets in the field of view. In such cases, the tracking could fail or require manual adjustments, reducing the automation of the process. Second, the alignment procedure relies on calculating the barycenter of the bright regions. If an image contains multiple bright objects or if the background noise is too high, this could lead to errors in estimating the relative displacement, affecting the quality of the final combination.

Finally, the code includes a step to replace pixels outside the dynamic range after the combination. This feature effectively corrected anomalies in the tested images but could introduce a bias if entire regions are saturated or out of range. An improvement could be to detect and exclude these regions before the combination.

4 Conclusion

Writing this notebook allowed me to design a simple and accessible tool for processing images obtained with Telesto. Although the code is not perfect and does not handle some advanced automations found in specialized libraries, it fulfills its purpose: offering a practical and fast solution for processing a variable number of images, while remaining user-friendly.

This project gave me the opportunity to dive deeper into astrophotography, a field that fascinates me, while also developing my coding skills, an area still relatively new to me. It enabled me to better understand the challenges faced by professional image processing software, whose algorithms are often complex and opaque. Designing this notebook thus provided me with a clearer vision of the challenges involved in astronomical image processing.

It also made me realize that image processing has its limitations and that the quality of the images is essential to facilitate processing. I learned a lot about instrumental limitations, such as the system's impulse response (or PSF, Point Spread Function), as well as light transmission, particularly through the study of filters and other factors influencing image quality.

4.0.1 Perspectives

This project represents an initial step towards the development of a more robust and adaptable astrophotography processing system. While it effectively meets the immediate needs of processing raw images, it paves the way for several avenues of improvement to refine the quality and accuracy of the results.

Among future directions, one could consider extending the code to support the correction of light pollution, such as that caused by satellites or airplanes passing in front of the telescope's lens. Additionally, to improve image precision and reduce distortions caused by the instruments, developing optical correction techniques would be pertinent. Finally, integrating astrophysical databases for image colorization would offer the possibility of achieving more accurate representations of celestial objects, contributing to a better interpretation of the observed data.

5 References

Alarcon, Miguel R. et al. (Jan. 2023). "Scientific CMOS sensors in Astronomy: QHY600 and QHY411". In: *2nd NEO and Debris Detection Conference*, 3, p. 3.

Ashley, Joseph (2015). "Astrophotography Basics". en. In: *Astrophotography on the Go: Using Short Exposures with Light Mounts*. Ed. by Joseph Ashley. Cham: Springer International Publishing, pp. 33–71.

Baader UBVRI Filter – Transmission - (2024). URL: `https://www.baader-planetarium.com/en/baader-ubvri-bessel-v-filter-photometric.html` (visited on 11/04/2024).

Eecke, P.V. et al. (1938). *L'optique et la catoptrique*. Desclée de Brouwer.

Galilei, Galileo (Jan. 2016). *Sidereus Nuncius, or The Sidereal Messenger*. en. University of Chicago Press.

Gillespie, Sarah Kate (Aug. 2012). "John William Draper and the Reception of Early Scientific Photography". In: *History of Photography* 36.3, pp. 241–254.

Gruen, D. et al. (Feb. 2014). "Implementation of Robust Image Artifact Removal in SWarp through Clipped Mean Stacking". en. In: *Publications of the Astronomical Society of the Pacific* 126.936, p. 158.

Hayden, Brian et al. (Oct. 2011). "Astronomy in the Upper Palaeolithic?" fr. In: *Cambridge Archaeological Journal* 21.3, pp. 331–355.

Howell, Steve B. (Apr. 2000). *Handbook of CCD Astronomy*. en. Cambridge University Press.

Magnan, Pierre (May 2003). "Detection of visible photons in CCD and CMOS: A comparative view". In: *Nuclear Instruments and Methods in Physics Research Section A: Accelerators, Spectrometers, Detectors and Associated Equipment*. Proceedings of the 3rd International Conference on New Developments in Photodetection 504.1, pp. 199–212.

Marshack, Alexander (1964). "Lunar Notation on Upper Paleolithic Remains". In: *Science* 146.3645, pp. 743–745.

Merline, W. J. et al. (Jan. 1995). "A realistic model for point-sources imaged on array detectors: The model and initial results". en. In: *Experimental Astronomy* 6.1, pp. 163–210.

Ptolemy et al. (1996). *Ptolemy's Theory of Visual Perception: An English Translation of the Optics*. en. American Philosophical Society.

Topac, Ersah (Apr. 2018). "Design of a turbulent flow facility and development of an algorithm for PIV". PhD thesis.

6 Appendixes

6.1 Python libraries

- `astropy`, dedicated to astronomy and astrophysics, provides tools to read and process data files (such as FITS files), manage physical units, handle celestial coordinates, and perform cosmological calculations.
- `ccdproc`, designed for image processing (calibration, alignment, etc.) from CCD detectors.
- `numpy`, which allows for performing numerous mathematical operations on data arrays (the images, in our case).
- `matplotlib.pyplot`, a library used for graphical visualization of data.
- `pathlib`, which simplifies file path and directory manipulation in a portable and simple manner.
- `shutil`, which allows various file and directory operations such as copying, moving, and deleting.

6.2 Jupyter notebook

Access the Jupyter Notebook.